**Showcasing research from the Battery and Electrochemistry Laboratory (BELLA), Institute of Nanotechnology, Karlsruhe Institute of Technology (KIT), Germany.**

Transition-metal interdiffusion and solid electrolyte poisoning in all-solid-state batteries revealed by cryo-TEM

Scanning transmission electron microscopy investigations under cryogenic conditions into the degradation of thiophosphate-based all-solid-state batteries not only reveal interphase formation, due to side reactions between solid electrolyte and cathode material during cycling, but also transition metal dissolution and solid electrolyte poisoning.
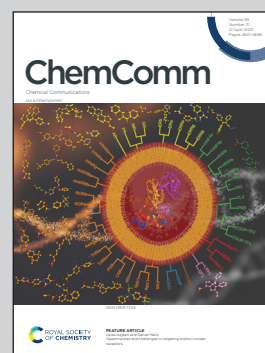
ROYAL SOCIETY
OF **CHEMISTRY**

rsc.li/chemcomm

Check for updates

Transition-metal interdiffusion and solid electrolyte poisoning in all-solid-state batteries revealed by cryo-TEM†

Ruizhuo Zhang, [a] Florian Strauss,*[a] Lin Jiang,[b] Lee Casalena,[b] Letian Li,[c] Jürgen Janek, [ad] Aleksandr Kondrakov[ae] and Torsten Brezesinski [a]

Using scanning transmission electron microscopy, along with electron energy loss spectroscopy, under cryogenic conditions, we demonstrate transition-metal dissolution from a layered Ni-rich oxide cathode material and subsequent diffusion into the bulk of a lithium thiophosphate solid electrolyte during electrochemical cycling. This problem has previously only been considered for liquid-electrolyte-based batteries.

Solid-state batteries (SSBs) hold great promise as a next-generation energy storage technology for powering future portable electronics and electric vehicles. This is due in part to their potentially superior energy and power densities and improved safety over conventional batteries.[1] However, commercial implementation is plagued by detrimental interfacial side reactions occurring at the cathode and anode, causing performance decay and ultimately cell failure.[2–5] Many efforts have been made to reveal the underlying degradation mechanisms and to prevent or alleviate such intrinsic problems.[6–8] The solid and gaseous degradation products formed during cycling at the interface between the cathode active material (CAM) and superionic solid electrolyte (SE) are usually probed using techniques such as X-ray photoelectron spectroscopy (XPS), time-of-flight secondary ion mass spectrometry (ToF-SIMS) and differential electrochemical mass spectrometry (DEMS).[5,9–12] The latter techniques, however, have limited spatial resolution capabilities. To gain detailed insights into the composition and structure

of the CAM/SE interface (decomposition interphase), transmission electron microscopy (TEM) appears to represent the method of choice.[13] Unfortunately, sulfide-based SEs are prone to beam damage (degradation),[14] and they are also highly reactive towards ambient atmosphere (moisture/oxygen), thereby complicating specimen preparation procedures.[15] To overcome these hurdles, sample handling under inert atmosphere and microscopy investigation, including TEM lamella sample preparation, at cryogenic temperature are required. Following this, here we study the evolution of the cathode interface/interphase in bulk-type SSB cells using a non-coated $LiNi_{0.85}Co_{0.1}Mn_{0.05}O_2$ (NCM851005) CAM and an argyrodite Li_6PS_5Cl SE *via* scanning TEM (STEM) in combination with energy-dispersive X-ray spectroscopy (EDS) and electron energy loss spectroscopy (EELS).

The cathode was prepared by slurry casting (see ESI,† for details) and tested in pellet-stack cells with a $Li_4Ti_5O_{12}$ anode. The areal CAM loading was around 9.4 mg cm^{-2}. Representative voltage profiles for the first and second cycles at a rate of 0.1C are depicted in Fig. 1a. They are typical of Ni-rich NCM CAMs. In the initial cycle, specific charge and discharge capacities of about 233 and 192 mA h g^{-1} were achieved, corresponding to a Coulomb efficiency (CE) of 82%. The cells delivered a similar capacity of $q_{dis} \approx 191$ mA h g^{-1} in the second cycle, and the CE increased to 98%. After the first two cycles, the rate capability was tested (Fig. 1b). To this end, the C-rate was increased in a stepwise manner from 0.2C ($q_{dis} \approx 179$ mA h g^{-1}) to 2C ($q_{dis} \approx 99$ mA h g^{-1}) (Fig. S1, ESI†), followed by cycling at 1C for 150 cycles. As can be seen from the data, there was no significant capacity fading over the first 160 cycles despite the absence of a protective surface coating on the CAM secondary particles. The CE stabilized above 99.9% during long-term cycling, with some decay towards 99.8% after around 100 cycles due to continuous (but relatively minor) SE decomposition.

For cryo-TEM analysis, cycled cells in the discharged state were disassembled and specimens from the cathode side were prepared by focused-ion beam (FIB) slicing. An illustration of

[a] Battery and Electrochemistry Laboratory, Institute of Nanotechnology, Karlsruhe Institute of Technology (KIT), Hermann-von-Helmholtz-Platz 1, Eggenstein-Leopoldshafen 76344, Germany. E-mail: florian.strauss@kit.edu, torsten.brezesinski@kit.edu

[b] Thermo Fisher Scientific, 5350 NE Dawson Creek Drive, Hillsboro, OR 97124, USA

*[c] Thermo Fisher Scientific, Achtseweg Noord 5, Eindhoven 5651 GG, The Netherlands*

[d] Institute of Physical Chemistry and Center for Materials Research, Justus-Liebig-University Giessen, Heinrich-Buff-Ring 17, Giessen 35392, Germany

[e] BASF SE, Carl-Bosch-Str. 38, Ludwigshafen 67056, Germany

† Electronic supplementary information (ESI) available. See DOI: https://doi.org/10.1039/d3cc00516j
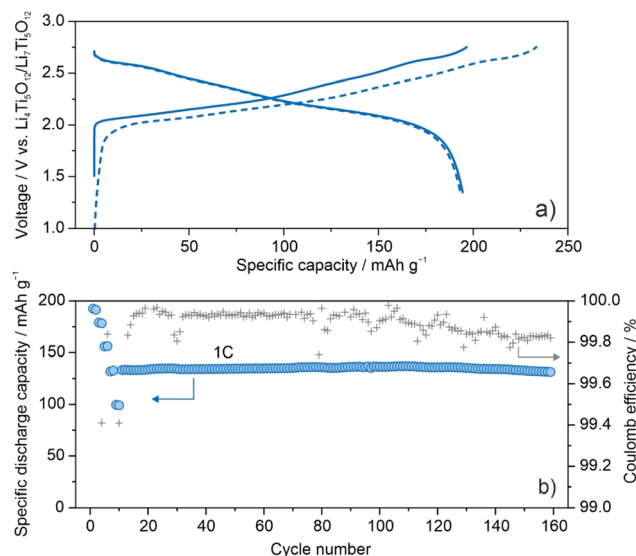
Fig. 1 Cycling performance of the slurry-cast cathode in pelletized SSB cells at 45 °C. (a) First- and second-cycle voltage profiles at 0.1C are shown as dashed and solid lines, respectively. (b) Specific discharge capacities over 160 cycles, including a rate capability test in the beginning of cycling (see ESI† for details), and corresponding Coulomb efficiencies.

the workflow process is shown in Fig. S2a–e (ESI†). Low-magnification images of a FIB-cut lamella are presented in Fig. S3a and b (ESI†), showing no signs of cracking or delamination. The interface region of interest (ROI) between CAM and SE, indicated by arrows in Fig. 2a, was probed using STEM [primarily in high-angle annular dark-field (HAADF) mode] and EDS. As shown in the inset of Fig. 2a, a mostly amorphous decomposition layer of approximate thickness 10 nm had formed after cycling. Such an interphase was not visible for the pristine cathode (Fig. S4a, ESI†). EDS mapping was conducted to reveal the elemental distribution across the CAM/SE interface (Fig. 2b). Both Ni and O are evenly distributed throughout the CAM particle (Fig. 2c and d), whereas the S and Cl maps show a non-uniform distribution (Fig. 2e and f). Increased signal intensity is evident near the interface region, which is corroborated by the O, S and Cl overlap map in Fig. 2g. The ion accumulation at the ROI originates from the (electro)-chemical SE decomposition during cycling (also considering oxygen release from the CAM at high states of charge), leading to the formation of LiCl, polysulfides and oxygenated phosphorus and sulfur species, to name some degradation products, as determined by XPS and ToF-SIMS in recent years.[9,12,16–18] This is in contrast to the pristine cathode, where clear spatial separation of elements points towards the presence of a well-defined ("clean") CAM/SE interface (Fig. S4b–f, ESI†).

EELS was conducted on three different spots, the CAM (P1), the CAM/SE decomposition interphase (P2) and the SE (P3), as can be seen in Fig. 3a. The corresponding energy loss spectra are depicted in Fig. 3b. For P1 and P2, the O K-, Mn L-, Co L- and Ni L-edges are clearly visible, and even for P3, weak signals pertaining to the transition metals (TMs) can be observed. This result suggests that TM dissolution occurs
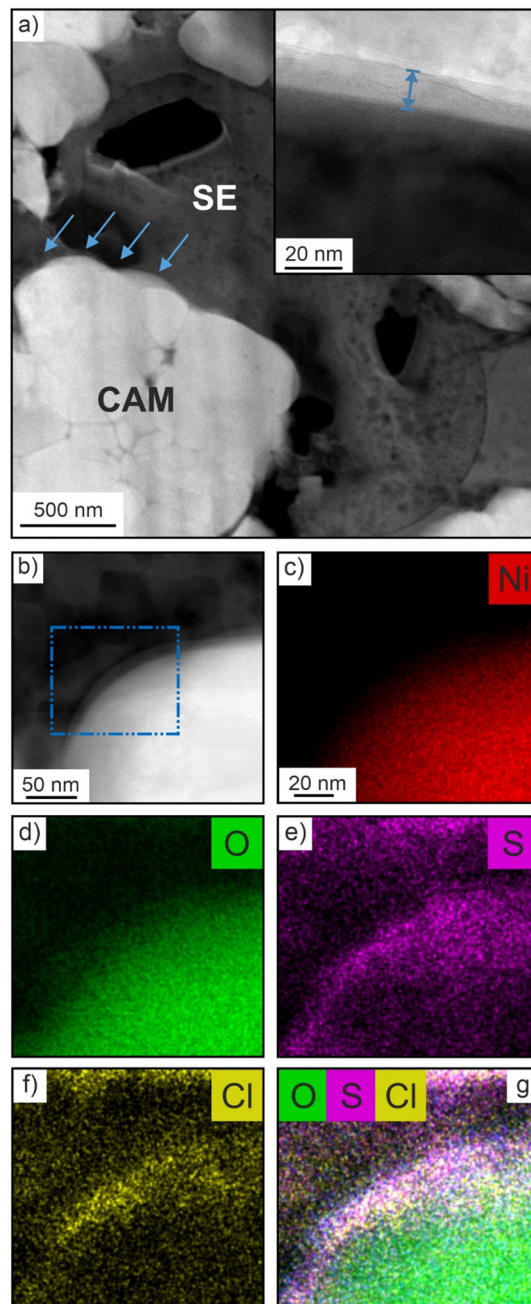
Fig. 2 Cross-sectional cryo-STEM/EDS analysis of the cycled cathode. (a) HAADF overview image showing both CAM and SE, with the interfacial ROI denoted by arrows. The inset is a high-magnification annular bright-field image of the decomposition interphase. (b) HAADF image of the CAM/SE interface and (c–g) elemental maps from EDS for Ni, O, S and Cl of the area indicated by the rectangle in (b).

during battery operation (apparent detection of TM species in the decomposition interphase and within the argyrodite SE). Note that the O K-edge is also detected for P3, either due to the presence of impurities or oxygen incorporation from the CAM, which is the only source of oxygen in the electrode. Wang et al. recently reported signs of TM dissolution into a $Li_{10}Si_{0.3}PS_{6.7}Cl_{1.8}$ SE, in agreement with our findings.[19]
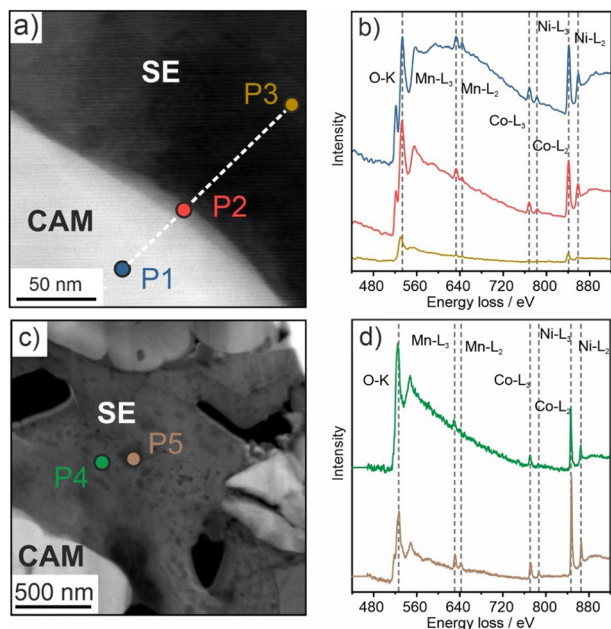
Fig. 3 (a) High-magnification HAADF image of the CAM/SE interface, with the highlighted areas probed by EELS, and (b) corresponding energy loss spectra. (c) Low-magnification HAADF image of the bulk SE in the cycled cathode and (d) corresponding energy loss spectra collected from the areas denoted in (c). The O K- and TM L-edges are indicated by dashed lines in the spectra.

To gain further insights into the morphological evolution of the cathode, low-magnification STEM images were taken prior to and after cycling. As is evident from the data in Fig. S5a and b (ESI†), the SE appearance changes from uniform to non-uniform with cycling. Brighter and darker areas/spots are visible all over the SE, hinting at different relative densities. For this reason, EELS was conducted on two representative areas, denoted as P4 (bright) and P5 (dark) in Fig. 3c. The K- and L-edges that can be assigned to O and Ni, Co and Mn, respectively, are apparent in the corresponding spectra in Fig. 3d. Because the areas probed were more than 500 nm away from the CAM secondary particles, this provides evidence for TM dissolution and subsequent diffusion into the bulk of the SE. In conventional liquid-electrolyte-based Li-ion batteries (LIBs), TM dissolution has been shown to be detrimental to the cycling performance by poisoning of the graphite anode, among others.[20–23] However, a similar effect in SSBs has not been reported yet. To compare the oxidation numbers for all of the TM species in the different areas, the EELS data were analyzed in some more detail. In particular, the L_3/L_2 ratios from the integrated peak areas were calculated (see ESI† for details and Fig. S6) for Mn, Co and Ni.[24,25] The results are given in Table S1 and depicted in Fig. S7 (ESI†). For the CAM (P1 in Fig. 3a), Ni/Co and Mn were determined to be in +3 and +4 state, respectively, as usually observed for Ni-rich NCM-type materials.[26] Both Ni and Co remained on average in +3 state in the CAM/SE interface region (P2 in Fig. 3a), whereas the slightly increased L_3/L_2 ratio for Mn suggests partial reduction towards mixed +4/+3 states. In contrast, for the SE at a distance around

100 nm away from the interface (P3 in Fig. 3a), the L_3/L_2 ratio increased for all three TMs, especially for Co and Ni. This is indicative of distinct reduction of Co and Ni from originally +3 to +2 state. The data also suggest partial reduction of Mn to mixed +3/+2 states.[24,27,28] In the bulk SE (P4 and P5 in Fig. 3c), i.e., several hundreds of nanometers away from the interface, areas of different appearance/contrast were detected by STEM (Fig. S5a and b, ESI†), as described above. As expected, analysis of the L_3/L_2 ratios revealed differences in the oxidation numbers. Mn was found to be present in states ranging from +4 to +2 and Ni from +3 to +2. By contrast, Co was closer to +2 state. Taken together, the results corroborate the inhomogeneous nature of the SE after cycling. More in-depth characterization, including phase identification, is very challenging though. Nevertheless, it can be assumed that TM-containing oxide and sulfide species are formed.[3,9,19,29]

In addition, the difference in energy loss between the O K-edge and the pre-edge (referred to as ΔE hereafter) can be considered. As shown in Table S1, ΔE decreased from 12.0 eV for P1 (CAM) to 8.7 eV for P5 (bulk SE) [$\Delta E = 10.8$ eV for P2 (CAM/SE interface region)], thus confirming TM reduction upon dissolution/diffusion.[30]

Apart from that, we also noticed sulfur diffusion into the CAM secondary particles. Fig. 4a–d shows a high-magnification HAADF image of a fractured NCM851005 particle and elemental maps from EDS for Ni and S. The spectra collected from the different areas denoted in Fig. 4d reveal an increased sulfur signal for the grain boundary region (Fig. 4e), corroborating sulfur accumulation in the particle interior. We hypothesize that this is related to the mechanical degradation of the CAM and the (electro)chemical SE oxidation during cycling, leading to a loose grain boundary structure and formation of mobile species. Similar observations (Cl/P accumulation) have been made recently.[31,32]

In summary, we have demonstrated that not only interphase formation occurs at the CAM/SE contact points in thiophosphate-based SSBs, but also distinct TM dissolution and diffusion into the bulk of the SE. Although the dissolution (and migration/deposition) of TM species from NCM materials in liquid-electrolyte-based LIBs is a well-known and understood phenomenon, to our knowledge, it has not received attention in prior research on solid-state cells. Our data emphasize the highly dynamic nature of thiophosphate-based SSBs, with (electro)chemically driven solid-state interdiffusion reactions occurring during cycling. Taken together, the findings uncover a previously unknown degradation mechanism that needs to be considered in future SSB research and development. It may well be that TM interdiffusion is responsible, at least to some degree, for electro-chemo-mechanical degradation and fracture processes. Further studies are needed to clarify this (including elucidating the driving force for TM dissolution/diffusion) and also to determine if protective surface coatings on the CAM particles are capable of suppressing SE poisoning by preventing direct contact between CAM and SE. Apart from that, it is unclear if similar effects would occur in SSBs using organic, hybrid or other types of inorganic SEs (oxide, halide etc.).
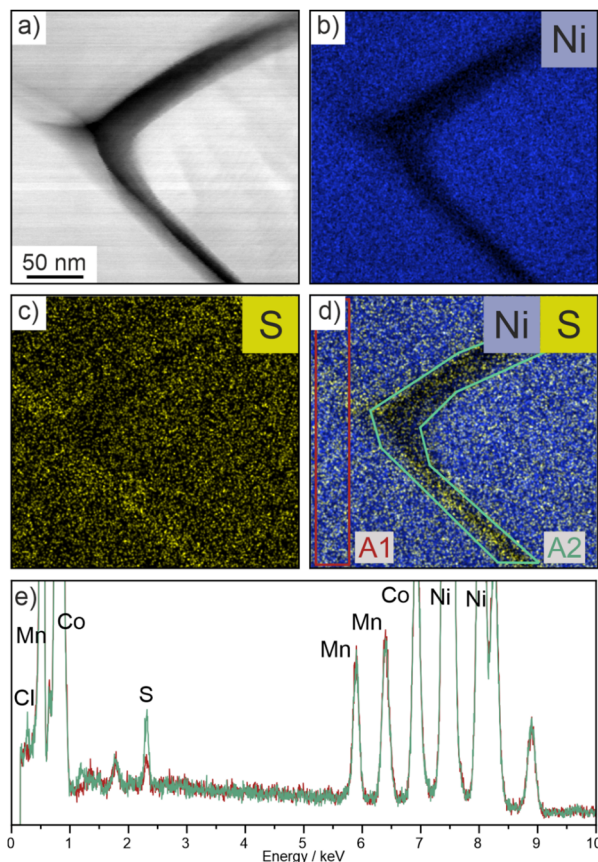
Fig. 4 (a) High-magnification HAADF image of a cycled CAM particle showing intergranular fracture and (b–d) corresponding elemental maps from EDS for Ni and S. (e) Spectra collected from the areas A1 and A2 indicated in (d).

Conflicts of interest

There are no conflicts to declare.

Notes and references

1 J. Janek and W. G. Zeier, *Nat. Energy*, 2016, **1**, 16141.
2 W. D. Richards, L. J. Miara, Y. Wang, J. C. Kim and G. Ceder, *Chem. Mater.*, 2016, **28**, 266–273.
3 Y. Xiao, Y. Wang, S.-H. Bo, J. C. Kim, L. J. Miara and G. Ceder, *Nat. Rev. Mater.*, 2020, **5**, 105–126.
4 R. Koerver, I. Aygün, T. Leichtweiß, C. Dietrich, W. Zhang, J. O. Binder, P. Hartmann, W. G. Zeier and J. Janek, *Chem. Mater.*, 2017, **29**, 5574–5582.
5 A. Banerjee, X. Wang, C. Fang, E. A. Wu and Y. S. Meng, *Chem. Rev.*, 2020, **120**, 6878–6933.
6 S. P. Culver, R. Koerver, W. G. Zeier and J. Janek, *Adv. Energy Mater.*, 2019, **9**, 1900626.
7 Y. Xiao, L. J. Miara, Y. Wang and G. Ceder, *Joule*, 2019, **3**, 1252–1275.
8 K. Kerman, A. Luntz, V. Viswanathan, Y.-M. Chiang and Z. Chen, *J. Electrochem. Soc.*, 2017, **164**, A1731–A1744.
9 F. Walther, F. Strauss, X. Wu, B. Mogwitz, J. Hertle, J. Sann, M. Rohnke, T. Brezesinski and J. Janek, *Chem. Mater.*, 2021, **33**, 2110–2125.
10 F. Strauss, J. H. Teo, A. Schiele, T. Bartsch, T. Hatsukade, P. Hartmann, J. Janek and T. Brezesinski, *ACS Appl. Mater. Interfaces*, 2020, **12**, 20462–20468.
11 A.-Y. Kim, F. Strauss, T. Bartsch, J. H. Teo, T. Hatsukade, A. Mazilkin, J. Janek, P. Hartmann and T. Brezesinski, *Chem. Mater.*, 2019, **31**, 9664–9672.
12 J. Auvergniot, A. Cassel, J.-B. Ledeuil, V. Viallet, V. Seznec and R. Dedryvère, *Chem. Mater.*, 2017, **29**, 3883–3890.
13 F. Strauss, D. Kitsche, Y. Ma, J. H. Teo, D. Goonetilleke, J. Janek, M. Bianchini and T. Brezesinski, *Adv. Energy Sustainability Res.*, 2021, **2**, 2100004.
14 F. Lin, I. M. Markus, M. M. Doeff and H. L. Xin, *Sci. Rep.*, 2014, **4**, 5694.
15 Y. Nikodimos, C.-J. Huang, B. Woldegbreal Taklu, W.-N. Su and B. Joe Hwang, *Energy Environ. Sci.*, 2022, **15**, 991–1033.
16 U.-H. Kim, H.-H. Ryu, J.-H. Kim, R. Mücke, P. Kaghazchi, C. S. Yoon and Y.-K. Sun, *Adv. Energy Mater.*, 2019, **9**, 1803902.
17 F. Walther, R. Koerver, T. Fuchs, S. Ohno, J. Sann, M. Rohnke, W. G. Zeier and J. Janek, *Chem. Mater.*, 2019, **31**, 3745–3755.
18 S. Kobayashi, H. Watanabe, T. Kato, F. Mizuno and A. Kuwabara, *ACS Appl. Mater. Interfaces*, 2022, **14**, 39459–39466.
19 Z. Wang, Z. Wang, D. Xue, J. Zhao, X. Zhang, L. Geng, Y. Li, C. Du, J. Yao, X. Liu, Z. Rong, B. Guo, R. Fang, Y. Su, C. Delmas, S. J. Harris, M. Wagemaker, L. Zhang, Y. Tang, S. Zhang, L. Zhu and J. Huang, *Nano Energy*, 2023, **105**, 108016.
20 Z. Xu, M. M. Rahman, L. Mu, Y. Liu and F. Lin, *J. Mater. Chem. A*, 2018, **6**, 21859–21884.
21 J. Wandt, A. Freiberg, R. Thomas, Y. Gorlin, A. Siebel, R. Jung, H. A. Gasteiger and M. Tromp, *J. Mater. Chem. A*, 2016, **4**, 18300–18305.
22 S. J. Wachs, C. Behling, J. Ranninger, J. Möller, K. J. J. Mayrhofer and B. B. Berkes, *ACS Appl. Mater. Interfaces*, 2021, **13**, 33075–33082.
23 W. Li, *J. Electrochem. Soc.*, 2020, **167**, 090514.
24 Z. L. Wang, J. S. Yin and Y. D. Jiang, *Micron*, 2000, **31**, 571–580.
25 Z. Wang, D. Santhanagopalan, W. Zhang, F. Wang, H. L. Xin, K. He, J. Li, N. Dudney and Y. S. Meng, *Nano Lett.*, 2016, **16**, 3760–3767.
26 F. Schipper, M. Dixit, D. Kovacheva, M. Talianker, O. Haik, J. Grinblat, E. M. Erickson, C. Ghanty, D. T. Major, B. Markovsky and D. Aurbach, *J. Mater. Chem. A*, 2016, **4**, 16073–16084.
27 N. Twu, M. Metzger, M. Balasubramanian, C. Marino, X. Li, H. Chen, H. Gasteiger and G. Ceder, *Chem. Mater.*, 2017, **29**, 2584–2593.
28 B. Serment, C. Brochon, G. Hadziioannou, S. Buffière, A. Demourgues and M. Gaudon, *RSC Adv.*, 2019, **9**, 34125–34135.
29 J. Haruyama, K. Sodeyama, L. Han, K. Takada and Y. Tateyama, *Chem. Mater.*, 2014, **26**, 4248–4255.
30 S. Hwang, S. Y. Kim, K. Y. Chung, E. A. Stach, S. M. Kim and W. Chang, *APL Mater.*, 2016, **4**, 096105.
31 Y. Ma, R. Zhang, Y. Tang, Y. Ma, J. H. Teo, T. Diemant, D. Goonetilleke, J. Janek, M. Bianchini, A. Kondrakov and T. Brezesinski, *ACS Nano*, 2022, **16**, 18682–18694.
32 K.-J. Lee, Y.-W. Byeon, H.-J. Lee, Y. Lee, S. Park, H.-R. Kim, H.-K. Kim, S. J. Oh and J.-P. Ahn, *Energy Storage Mater.*, 2023, **57**, 326–333.